Mechanism of Fermi Level Pinning for Metal Contacts on Molybdenum Dichalcogenide

Journal:	*ACS Applied Materials & Interfaces*
Manuscript ID	am-2023-18332p.R1
Manuscript Type:	Article
Date Submitted by the Author:	05-Feb-2024
Complete List of Authors:	Wang, Xinglu; The University of Texas at Dallas, Materials Science and Engineering Hu, Yaoqiao; The University of Texas at Dallas, Materials of Science & Enginnering Kim, Seong Yeoul; The University of Texas at Dallas, Materials Science and Engineering Cho, Kyeongjae; University of Texas at Dallas, Materials Science & Engineering Wallace, Robert; University of Texas at Dallas, Depy. of Materials Science and ENgineering

Mechanism of Fermi Level Pinning for Metal Contacts on Molybdenum Dichalcogenide

Xinglu Wang[1], Yaoqiao Hu[1], Seong Yeoul Kim[1], Kyeongjae Cho[1], and Robert M. Wallace[1,]*

[1] Department of Materials Science and Engineering, The University of Texas at Dallas, Richardson, TX 75080, United States of America

ABSTRACT: The high contact resistance of transition metal dichalcogenide (TMD) -based devices is receiving considerable attention due to its limitation on electronic performance. The mechanism of Fermi level (E_F) pinning, which causes the high contact resistance, is not thoroughly understood to date. In this study, the metal (Ni and Ag)/Mo-TMDs surfaces and interfaces are characterized by X-ray photoelectron spectroscopy, atomic force microscopy, scanning tunnelling microscopy and spectroscopy, and density functional theory systematically. Ni and Ag form covalent and van der Waals (vdW) interfaces on Mo-TMDs, respectively. Imperfections are

[1] Email: rmwallace@utdallas.edu

detected on Mo-TMDs, which leads to electronic and spatial variations. Gap states appear after the adsorption of single, and two metal atoms on Mo-TMDs. The combination of the interface reaction type (covalent or vdW), the imperfection variability of the TMD materials, and the gap states induced by contact metals with different weights are concluded to be the origins of E_F pinning.

KEYWORDS: transition metal dichalcogenide, metal contact, Fermi level pinning, interface chemistry, band alignment, surface imperfections, adsorption

1. INTRODUCTION

Transition metal dichalcogenides (TMDs), a family of layered two-dimensional materials, have demonstrated great potential for application in various electronic devices.[1-3] However, the high contact resistance (R_C) for the metal/TMD interface is one of the bottlenecks that limit the improvement of the electronic performance for TMD-based devices.[4] To understand the mechanism of this high R_C, various metal contacts have been employed for Mo-TMD transistors to investigate the Fermi level (E_F) pinning effect. The processing conditions, such as the metal deposition condition,[5-7] the substrate holding the TMD flake,[8] the physically adsorbed molecules,[9-10] the fabrication method of the TMD,[11] and their defect density,[12-13] could modify the band alignment of a metal/TMD interface and lead to variable contact performance.[14] The gap states at

the metal/TMD interface induced by direct metal deposition are also reported to cause E_F pinning and lead to the formation of Schottky contacts for both covalent and van der Waals (vdW) contact interfaces.[15-17] In addition, the strain[18-19] and the interface dipole[20-21] at the metal/TMD interface could also contribute to the E_F pinning.

Based on the information presented above, it becomes evident that the underlying causes of E_F pinning cannot be exclusively attributed to a single previously mentioned viewpoint. In the context of a specific metal/TMD interface, the phenomenon of E_F pinning arises as a result of a combination of various factors. This is further supported by the variation in R_c values observed across different research groups, even when using the same metal and TMD combination.[22] This underscores the pressing need to explore the fundamental principles and the significance of each contributing factor. The complexity arising from the coexistence of these factors necessitates a comprehensive and systematic investigation to unravel the fundamental physics and chemistry behind the E_F pinning of metal contacts on TMDs.

Recently, metals, such as Bi, Sn, In, and Sb, with low melting temperature and high vapor pressure demonstrate record low contact resistance with TMD materials.[23-27] The semi-metallic nature and the reduced damage (e.g., bond scission, defect generation and modification[28-29]) to the

TMD during metallization are attributed to the improved electronic performance. However, the low melting temperature of these metals (Bi: 271.40 ℃, Sn: 231.93 ℃, In: 156.60 ℃, Sb: 630.63 ℃) and their diffusive nature would cause reliability and stability concerns for the back-end-of-line process.[30-32] Among the thermally stable metals, Ni (1455℃, R_c = 500 Ω·μm) and Ag (961.78℃, R_c = 180 Ω·μm) have shown promising contact performance on MoS_2.[33-34] It has been uncovered that the promising performance originates from the formation of the uniform covalent Schottky contact and the island vdW Ohmic contact for Ni and Ag, respectively.[12] In addition, their distinct interface types, covalent or vdW, with TMDs make them perfect candidates to understand the origin of E_F pinning by comparing the two cases at the same processing conditions.[35]

This work investigates the mechanism of E_F pinning in various aspects, including the interface chemistry, the electronic variability of TMDs, the band alignment, and the effect of contact metal adsorption for metal/Mo-TMD systems. More specifically, the interface chemistry between metal films (1 nm Ni and Ag) and exfoliated $MoSe_2$ and $MoTe_2$ bulk crystals is explored by X-ray photoelectron spectroscopy (XPS) with the variance of metal deposition ambient. The band alignment of a metal/TMD interface is extracted from the core level shift after the metal deposition under UHV and HV conditions. The electronic and spatial variations, caused by the imperfections

of Mo-TMDs, are characterized by scanning tunneling microscopy/spectroscopy (STM/STS). The contact metal adsorption mechanism and its effect on the electronic structure of the Mo-TMDs are simulated by density functional theory (DFT). The growth mechanisms of metal films, characterized by atomic force microscopy (AFM), are correlated to the interface reaction and the adsorption mechanism. The mechanism of E_F pinning is discussed in the aspects of interface chemistry, band alignment, variabilities and imperfections of the TMD materials, and the adsorption mechanism of contact metals as well as their effect on the metal-induced gap states (MIGS).

2. RESULTS AND DISCUSSION

2.1. Interface Chemistry of Metal Contacts on Mo-TMDs

Figure 1 presents the XPS and AFM results of the Ni, Ag/$MoSe_2$ systems after exfoliation and subsequent metal depositions under UHV and HV conditions.

Ni Contact. In Figure 1a, the appearance of the $Ni_xMo_ySe_z$ intermetallic state in the Mo 3d and Se 3d spectra indicates the formation of the reaction product at the Ni/$MoSe_2$ interface after Ni deposition. This interface reaction is consistent with the previously reported Ni reduction of MoS_2 regardless of the deposition ambient and the number of MoS_2 layers.[12] The detection of MoO_x

indicates the oxidation for the HV sample, which is consistent with the oxides detected in the Ni $2p_{3/2}$ and O 1s spectra as shown in Figure S1. Island-free, smooth surfaces, with Root Mean Square (RMS) roughness ≤ 0.1 nm, are obtained from Ni/$MoSe_2$ surfaces after HV and UHV Ni depositions by *ex-situ* AFM as shown in Figure 1b and c, suggesting that Ni tends to react with $MoSe_2$. The covalent interface also forms at the Ni/$MoTe_2$ interface as shown in Figure S2. Therefore, taken together, the XPS and AFM results indicate that a covalent interface forms at a Ni/Mo-TMD interface regardless of the deposition ambient.

Ag Contact. In contrast, the absence of any additional state after Ag deposition under UHV and HV conditions indicates the reaction between Ag and $MoSe_2$ is below the detection limit of XPS, as shown in the Mo 3d and Se 3d spectra (Figure 1d). The full width at half maximums (FWHMs) of Mo $3d_{5/2}$ and Se $3d_{5/2}$ peaks stay almost the same compared to those without Ag film (Table S1). The FWHM of Ag 3d is also close to the values of Ag thick film (~ 30 nm) and foil (Table S3). This outcome indicates the reaction between Ag and $MoSe_2$ is below the detection limit of XPS at the Ag/$MoSe_2$ interface regardless of the deposition ambient. The Ag islands detected by AFM after Ag depositions indicate the Volmer-Weber growth of Ag on $MoSe_2$, as shown in Figure 3b and c. The formation of a vdW interface between Ag and $MoTe_2$ is also observed (Figure S3).

This suggests that a vdW contact interface is formed at the Ag/Mo-TMD interface. The interface chemistry between metal contacts (Ni, Ag) and TMDs ($MoSe_2$, $MoTe_2$) is summarized schematically in Figure 2a.

2.2. Band Alignment

Band alignments between the metal contacts (Ni and Ag) and TMD ($MoSe_2$ and $MoTe_2$) bulk crystals are obtained from the shifts of the Mo-TMD peaks in the Mo 3d spectra after metal depositions relative to the reference.[36] The binding energies of the states detected in the Mo 3d, Se $3d_{5/2,}$ and Te 3d core level spectra are listed in Table S4. The electron affinities and ionization energies displayed in Figure 2b are consistent with those employed in the references.[6, 12, 36] The E_Fs of metal contact/TMD interfaces are presented before and after metal depositions in UHV and HV. (Figure S4 in the supporting information includes the band alignment of 2L-MoS_2 CVD film and MoS_2 bulk crystal reported elsewhere for comparison.[12]) The E_F results after *in-situ* metal deposition in UHV are considered the intrinsic value since any absorbed adventitious carbon and oxidation of the metal contacts during the *ex-situ* HV deposition and transfer process could potentially change the E_F at the metal/TMD interface.[37] Compared to the binding energy of the TMD bulk crystal state before metal deposition, a negative shift of the Mo 3d spectrum after metal

deposition indicates the increase of the work function at the metal contact/TMD interface. The band bending of the metal/TMD surface is negligible, considering that the depletion width of a semiconductor is much wider than the XPS sampling depth.[20]

The E_Fs of Ni/TMD interfaces are pinned close to the middle of the bandgap of the $MoSe_2$ and $MoTe_2$ bulk crystals. The observed E_F pinning is likely due to the $Ni_xMo_ySe_z$ and $Ni_xMo_yTe_z$ intermetallic reaction products detected in the core level spectra. The formation of interface dipole due to the charge redistribution could also contribute to the E_F pinning of the Ni/TMD interfaces.[38] The E_Fs of TMDs after Ag deposition in UHV are close to the intrinsic E_Fs without metal deposition. The E_F pinning probably originates from the defects and impurities of the TMD bulk crystals.[12] The effect of defects and impurities on the E_F pinning is going to be discussed in section 2.3, in which the imperfections of the TMDs are observed by STM/STS. For Ag/$MoTe_2$ bulk crystal interface, the Schottky barrier height extracted from the XPS result (0.16 eV) is in good agreement with the device result (0.29 eV) by transfer length measurement.[39] This consistency highlights the importance of interface chemistry study in the understanding of the origin of E_F pinning for metal contact/TMD systems. Compared to that of the UHV Ag/$MoTe_2$ sample, a greater Schottky barrier height is detected for the Ag/$MoTe_2$ bulk sample deposited under HV

conditions. This finding explains the improved contact performance in metal/TMD systems by employing the UHV deposition conditions.[5] The vdW gap between Ag and Mo-TMDs could result in the decay of the current injection at the metal/TMD interface although Ag shows promising band alignment with Mo-TMDs. In this point of view, forming a covalent contact between Ag and Mo-TMDs by the thermal treatment could be a potential strategy for achieving optimized contact with low resistance.

2.3. Imperfections of Mo-TMDs

Electronic and Spatial Variations. Figure 3 shows the STM images of freshly exfoliated $MoSe_2$ (a and b) and $MoTe_2$ (d and e) bulk crystal surfaces. The scan area is the same for a and b, as well as for c and d. The oxidation of these two samples is minimized as shown in the XPS results in Figure S5 and S6. In Figure 3a, concaves are present on the surface of $MoSe_2$. By changing the polarity of the sample bias from 0.85 V to -0.85 V, a concave could stay as a concave as shown in the white circle. In contrast, in the white square, protrusions show up at -0.85 V instead of a concave at 0.85 V. The phenomenon above indicates that an acceptor at a positive bias may serve as an acceptor or a donor at a negative bias. This indicates the electronic variation of the imperfections on the surface of $MoSe_2$. McDonnell *et al.* attribute the bright defects at negative

bias as metallic-like defects on MoS_2, leading to the inhomogeneous doping of the TMDs.[13] A local high contrast area in the positive bias, likely due to the impurities,[40-41] disappears at the negative bias as shown in the blue circle in Figure 3a and b. The surface topography also varies with the location on the surface of $MoSe_2$ as shown in Figure S7. The blue STS curve in Figure 3c is measured at the blue spot in Figure S7c. It indicates that this $MoSe_2$ surface is n-type with a bandgap of ~ 1.09 eV.[42] The same value is measured in Figure S7a and b for a less n-type area. However, a much smaller bandgap of ~ 0.54 eV is obtained in the area shown in Figure 3a and b. In Figure 3c, the STS intensity is not zero within the band gap of $MoSe_2$. This indicates the appearance of gap states, suggesting a doping effect of the impurities and defects, which is consistent with the strong n-type behavior.

The surface of $MoTe_2$ shows a significantly different topography to $MoSe_2$ as shown in Figure 3d and e. By changing the sample bias while fixing the scan area, similarities between the two images are not obvious in Figure 3d and e. This phenomenon, which is likely due to the TeO_x detected by XPS (Figure S6), is also observed in another area on the surface of $MoTe_2$ with gap states close to the conduction band as shown in Figure S8. In Figure 3f, the bandgap of $MoTe_2$ is measured to be ~ 1.02 eV.[43] The blue curve is more n-type compared to the green curve. This

indicates a heterogeneous doping effect by the imperfections, such as vacancies, antisites, impurities, and excessive chalcogen atoms at different locations within a 100 nm * 100 nm area, which is also reported for other TMD systems, such as MoS_2 and WSe_2.[13, 40, 44] The inhomogeneous distribution of the imperfections is probably responsible for the spatial, and electronic variations.

Atomic Defects. Atomic imperfections of $MoSe_2$ are characterized by STM and STS as shown in Figure 4. Single (white circle) and multiple (blue circle) Se vacancies (V_{Se}) are observed in Figure 4a. In Figure 4c, the depth of the multiple V_{Se} is measured to be ~ 1.7 Å along the green line in Figure 4a, which is consistent with the height of 0.5 layers of $MoSe_2$, as shown in the side view of the crystal lattice of $MoSe_2$ in Figure 4e. The O substitution of the chalcogen atom ($O_{Chalcogen}$), which shows very similar STM topography with V_{Se}, can also contribute to these dark point defects and the variations.[41, 45-46] Local high contrast (white arrow) and depression (black arrow) are detected in a vacancy-free area as shown in Figure 4b. This suggests the existence of impurities, like Re, Cr, V, Nb, etc., that would behave as dopants on the surface of $MoSe_2$.[41, 47-48] Similar bright and dark defects are attributed to V_{Se} and Se_{Pt} antisite on chemical vapor transport grown $PtSe_2$.[49] The lattice constant of $MoSe_2$ is ~3.29 Å as shown in the profile (Figure 4d) along the blue line in Figure 4b. This value is consistent with the results measured by X-ray diffraction

and transmission electron microscopy.[50-51] Figure 4g, h, and j show the defective $MoSe_2$ surface with various atomic defects, such as depressions (green arrow), bright defects within/on the edge of a depression (blue arrow), amorphous defects (black circle), surface V_{Se} or O_{Se} (white circle). Schuler *et al.* have reported that C, N, and CH substitution of S could also contribute to the depression and vacancy defects on the WS_2 surface.[50] Although the bonding of C or N with Mo is below the detection limit of XPS as shown in Figure S5 and S6, the adsorption of carbon species may deplete the surface carriers, leading to depressions on the surface. Various kinds of defects are also detected on the surface of $MoTe_2$ after exfoliation as shown in Figure S9a and S10b-d. The depth of V_{Te} or O_{Te} (Figure S9c), lattice constant (Figure S9d), and vacancy-free area (Figure S9b and S10a) of $MoTe_2$ are also included. The STS curve taken at the amorphous defect in Figure 4g shows a metallic behaviour without an obvious bandgap as illustrated in Figure 4i. This confirms that the defects of the TMDs would introduce variabilities to the electronic properties of the TMD materials, such as gap states, and doping effect.[13, 40, 44] For a TMD-based transistor, these imperfections could behave as dopants, traps, and scattering centers, which would significantly impact their electronic performance.

2.4. Metal contact atom adsorption mechanism

DFT calculations were performed to investigate the surface chemistry between deposited contact metal atoms and Mo-TMDs. For a single adatom, the adsorption energy is calculated for the three adsorption configurations: the Mo top, the chalcogenide top, and the hollow site. Figure 5a-d presents the atomic structures of Ag or Ni adsorbed on $MoSe_2$ or $MoTe_2$ with different adsorption configurations and their corresponding adsorption energies. The adsorption energy of the most stable site for each system is highlighted in pink. Ag preferably adsorbs on the hollow site while Ni prefers the Se/Te-top site.[52] At the hollow site, a single Ag adatom interacts with all three neighboring Mo atoms and three neighboring Se/Te atoms. Whereas for single Ni at the Mo-top site, it bonds with one Mo atom and three neighboring Se/Te atoms. The competition between Ni/Ag adatom-Mo bonding and Ni/Ag adatom-chalcogenide interaction determines the most energy-favorable adsorption site. Ni shows significantly stronger adsorption than Ag for all the sites,[53] on both $MoSe_2$ and $MoTe_2$, which is consistent with the experimental observation that Ag tends to form a vdW interface with TMDs while Ni forms a covalent interface. In addition to single adatom adsorption, two adatoms are also modeled to reveal the interaction between contact metal atoms on Mo-TMDs (Figure 5e). For two adatoms, each Ni atom would stay on the Se/Te-top site, like the single Ni adatom adsorption behavior. The adsorption energy for two Ni adatoms is twice

that for a single Ni adatom, for example, -7.05 eV versus -3.47 eV on $MoSe_2$. This suggests that Ni, on the surface of $MoSe_2$, shows negligible Ni-Ni interaction. In contrast, when two Ag atoms are adsorbed on Mo-TMDs, they move toward each other. Their adsorption energy is more than three times that of a single adatom (-2.41 eV versus -0.68 eV on $MoSe_2$). This implies considerable interaction between Ag adatoms. This simulated energy trend agrees with the experimental result that Ag forms islands while Ni forms a uniform film on Mo-TMDs. We have also calculated the electronic structure of Ni/Ag adsorbed Mo-TMDs, as shown in Figure 5f-i. The adsorbed single or two atom(s) alter the DOS of Mo-TMDs, such as new gap states and modified band edges. Ni modifies the DOS more than Ag for single and two adatoms on both $MoSe_2$ and $MoTe_2$. This further confirms that Ni shows a stronger orbital hybridization with Mo-TMDs than Ag. For a contact metal/TMD interface, the MIGS would deviate the band alignment from the Schottky-Mott rule and contribute to the E_F pinning.[38, 53] For the two Ag adatoms/$MoTe_2$ system, only the band edges are slightly modified, indicating that a vdW metal would induce fewer MIGS to the TMDs than a covalent metal contact. This explains the origin of record low R_C achieved by vdW contacts, such as Bi and In.[23-27] Although a bulk metal contact would induce much more abundant gap states than single or two adatoms, this trend that a vdW metal induces fewer MIGS should persist.[38]

2.4. Discussions

The Schottky-Mott rule has been widely used to predict band alignment at a metal/semiconductor interface.[54] However, the complicated nature of the metal/TMD interface and the variability of the TMD materials leads to the discrepancy between the experimental results and the theoretical prediction for the band alignment.[55] For example, in this study, both $MoSe_2$ and $MoTe_2$ are n-type after exfoliation due to the doping effect from the imperfections. For vdW Ag metal contacts, without interface reaction with $MoSe_2$ and $MoTe_2$, the E_F of the Ag/Mo-TMD interface is very close to their intrinsic E_F. This means that the defects and impurities of the Mo-TMDs play a significant role in E_F pinning, especially for vdW contacts. In contrast, covalent Ni contacts shift the E_Fs toward the valence band of the Mo-TMDs. This indicates that the strong interface interaction between Ni and Mo-TMD, together with the defects and impurities, leads to E_F pinning. Even after single and two contact metal atom(s) adsorption, MIGS and(or) modified band edge are observed for all the systems studied in this work. Therefore, the MIGS induced by bulk metal contacts, which would cause much stronger orbital hybridization than the single and two adatom(s) models, also needs to be included for the origins of E_F pinning at a metal/TMD interface.[38, 53] The deviation of the E_Fs for UHV *in-situ* and HV *ex-situ* Ag/$MoTe_2$ system is much

more obvious than the other systems. This indicates that the processing conditions, such as the deposition ambient, photolithography process, and sample transfer process, are crucial for air sensitive TMDs, especially for tellurides.[5, 9, 17]

3. CONCLUSIONS

This work studies the mechanism of E_F pinning for covalent Ni and vdW Ag contacts on Mo-TMDs in the aspects of interface chemistry, band alignment, imperfections of Mo-TMDs, and the effect of contact metal adsorption. The E_F pinning at a metal/TMD interface is a combination of the interface reaction type (covalent or vdW), the spatial and electronic variabilities of the TMDs, and the MIGS with different weights. The contact metal needs to be carefully chosen by not only the work function but also their reactivity nature and orbital hybridization with the TMDs. In addition, the imperfections (vacancies, antisites, impurities, crystallinity, etc.) of the TMD materials require enormous optimization to fabricate homogeneous TMDs with high quality to minimize the spatial and electronic variabilities. The band alignment discrepancy for the HV Ag/$MoTe_2$ interface highlights the importance of carefully engineering the processing conditions (e.g., metallization conditions, 2d film transfer process, the residue of the photoresist, etc.) of the TMD transistors to achieve reliable, reproducible, and manufacturable low dimensional devices.

These findings unveil the mechanism of E_F pinning systematically and guide in achieving Ohmic contact on TMDs with low contact resistance.

4. Experimental Methods

4.1. Metal deposition

$MoSe_2$ and $MoTe_2$ bulk crystals (~2 mm × 2 mm), purchased from HQ Graphene,[56] were affixed, side by side, on a 4-inch Si wafer by carbon tape to facilitate deposition and analysis. Within 1 min of the exfoliation, the sample assembly was loaded into the electron beam deposition systems for contact metal depositions. A target thickness of ~ 1 nm Ni and Ag films were deposited on the freshly exfoliated bulk crystals under UHV conditions, respectively. After contact metal depositions under UHV conditions (base pressure = ~ 3×10^{-11} mbar), the samples were *in-situ* transferred through a UHV tube to the XPS chamber without air exposure. More detailed descriptions of the *in-situ* cluster tool can be found elsewhere.[57] Contact metals were also deposited on exfoliated $MoSe_2$ and $MoTe_2$ bulk crystals under HV conditions (base pressure = ~ 3×10^{-6} mbar) using an elastomer-sealed Cryo electron beam evaporator in the cleanroom facility.[58] After metal depositions in HV, the samples were transferred to the cluster tool *ex-situ* for XPS characterizations. The air exposure during this *ex-situ* transfer process is ~ 5 mins. The *in-situ* and

ex-situ deposition and transfer processes were identical to our previous metal/TMD interface studies.[7] Therefore, a direct comparison with those studies could be performed readily. The method of obtaining the reference Ni $2p_{3/2}$ and Ag 3d spectra was described in our previous work.[12]

4.2. XPS

The XPS characterization was performed via a monochromatic Al Kα X-ray source ($h\nu$ = 1486.7 eV) and an Omicron EA125 analyzer with a pass energy of 15 eV for core level scans. The EA125 analyzer was calibrated according to the standard ASTM procedure using sputter-cleaned Au, Ag, and Cu foils.[59] The XPS spectra were obtained at the take-off angle of 45˚ with 0.05 eV energy resolution. The AAnalyzer software was employed for core-level peak fitting.[60] To make the fitting results consistent, congruent fitting parameters (the background type, the peak shape, the doublet separation, and the Gaussian and Lorentzian components of the peak width) were employed for a specific core level peak.[61] The scanning spot size for XPS acquisition is 1.5 mm, which is close to the size of the TMD crystal. Most of the adventitious carbon signal is probably from the exposed carbon tape.

4.3. AFM

AFM images of the $MoSe_2$ and $MoTe_2$ bulk crystals after metal depositions were obtained *ex-situ* by Veeco model 3100 Dimension V and Oxford Asylum Research Jupiter XF instruments in the tapping mode.[58] Image processing and root mean square (RMS) roughness determination were performed via the WSxM software.[62]

4.4. STM/STS

An Omicron VT-AFM system was used for STM/STS characterizations at the constant current mode at room temperature. To enhance the signal-to-noise ratio, at least 16 repetitions were averaged for every STS spectrum. Gwyddion software was used for image processing.[63] The conduction band and valence band edges are identified by the onset of a sudden increase in a differential conductance (dI/dV) spectrum. The $MoSe_2$ and $MoTe_2$ bulk crystals were exfoliated in air, after which the samples were loaded in the load lock within 1 min.

4.5. DFT calculations

DFT calculations were carried out by using the Vienna Ab initio Simulation Package (VASP) , which uses projected augmented wave (PAW) pseudopotentials.[64-67] Electronic exchange and correlation interaction are described by generalized gradient approximation (GGA-PBE) functional Perdew-Burke-Ernzerhof format (GGA-PBE).[68-69] For plane wave basis expansion, a

cutoff energy of 520 eV was used. Supercells were used with Gamma-only *k*-point mesh for Brillouin-zone sampling. For structure relaxation, the conjugated gradient method was employed, with the convergence criterion of the force on each atom less than 0.01 eV/Å. Self-consistent electronic minimization was achieved by using a blocked Davidson iteration scheme with energy converges at 10^{-5} eV. For surface adsorption modeling, metal adatoms were on top of the TMD surface. Adsorbed metal atoms were then relaxed with atoms in the TMD layer kept fixed. A 15-Å-thick vacuum region was introduced to minimize the interaction between adjacent periodic images. The adsorption energy was calculated according to $E_{ad} = E(\text{M/TMD})-E(\text{TMD})-E(\text{M})$, where E(M/TMD) is the energy of metal adsorbed TMD, E(TMD) and E(M) are energies of isolated TMD and metal atom(s) before adsorption, respectively.

ASSOCIATED CONTENT

Supporting Information. The experimental methods of this work; The XPS spectra of Ni/$MoSe_2$ and Ag/$MoSe_2$; Interface chemistry and surface morphology of Ni/$MoTe_2$ and Ag/$MoTe_2$; The FWHMs of the TMD states and Ag metal state; The binding energies of Mo-TMD states in the Mo $3d_{5/2}$, Se $3d_{5/2}$, and Te 3d spectra; Comparison of the band alignment for MoS_2, $MoSe_2$, and

$MoTe_2$; XPS spectra of the freshly exfoliated $MoSe_2$, and $MoTe_2$ for STM/STS; Spatial and electronic variations of $MoSe_2$ and $MoTe_2$ by STM/STS; Atomic imperfections of $MoTe_2$ by STM.

AUTHOR INFORMATION

Corresponding Author

E-mail: rmwallace@utdallas.edu. Phone: +1 (972) 883-6638.

Notes

The authors declare no competing financial interest.

ACKNOWLEDGMENT

This work was supported in part by NEWLIMITS, a center in nCORE, a Semiconductor Research Corporation (SRC) program sponsored by NIST through award number 70NANB17H041, and by the National Science Foundation through award DMR-2002741.

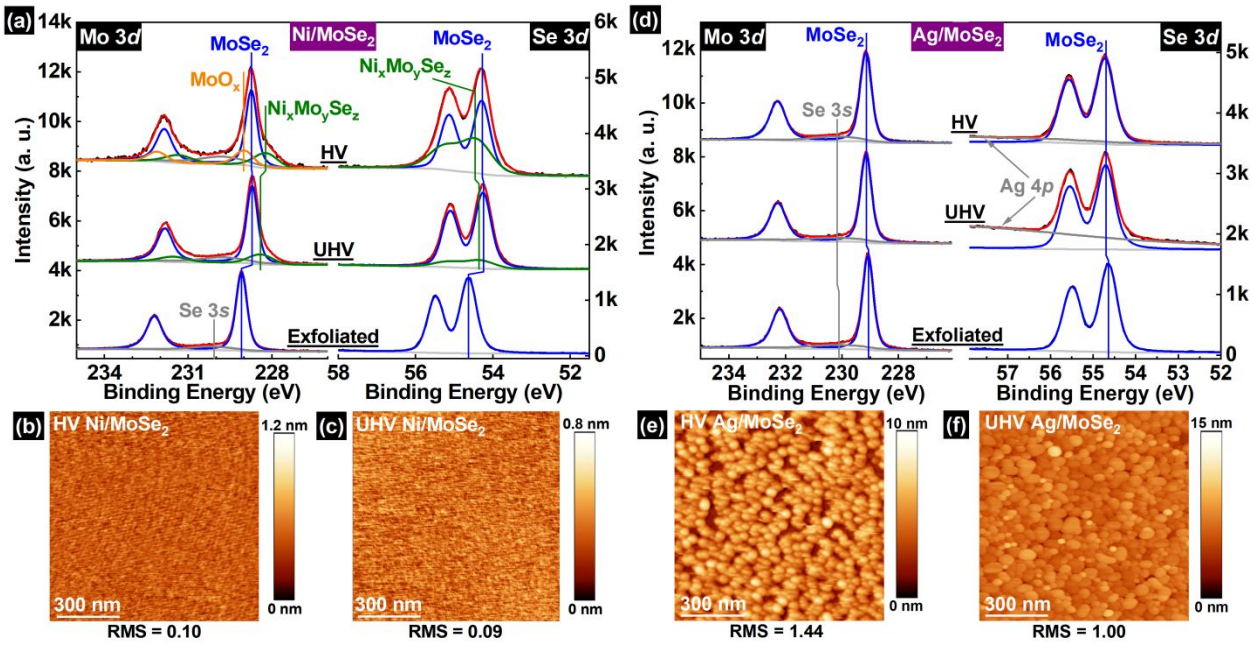

Figure 1. Mo 3d and Se 3d spectra of $MoSe_2$ bulk crystal following exfoliation and subsequent (a) Ni, and (d) Ag depositions under UHV and HV conditions. AFM results of Ni/$MoSe_2$ bulk crystal surfaces deposited under (b) HV and (c) UHV conditions. AFM results of Ag/$MoSe_2$ bulk crystal surfaces deposited under (e) HV and (f) UHV conditions. The unit of RMS roughness is nm.

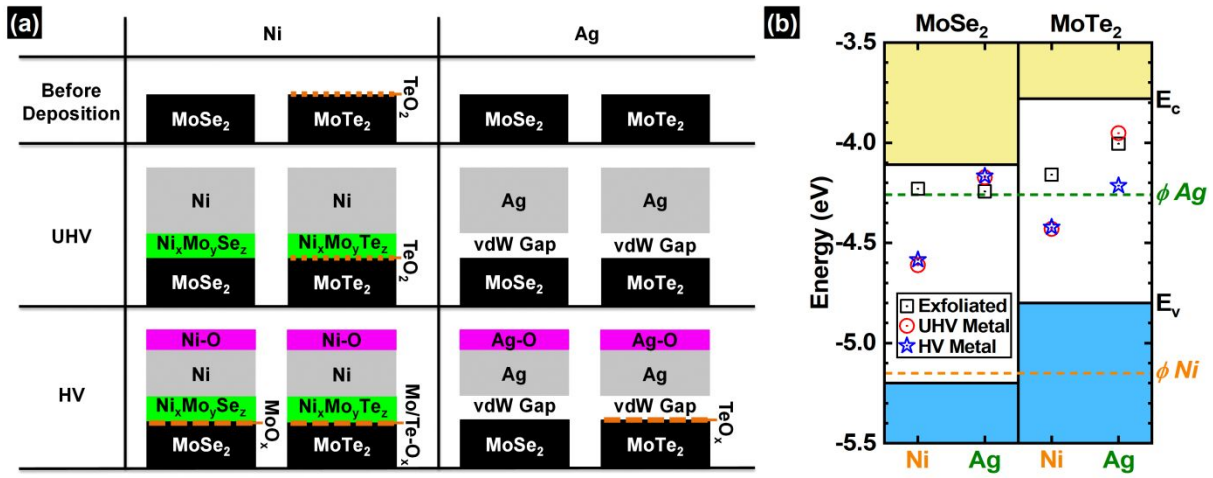

Figure 2. (a) Schematic representations of the interfaces formed between contact metals (Ni and Ag) and TMDs ($MoSe_2$ and $MoTe_2$) before and after metal depositions under UHV and HV conditions. (b) Band alignment of contact metal/TMD bulk crystal systems studied in this work after exfoliation and subsequent metal deposition under UHV and HV conditions.

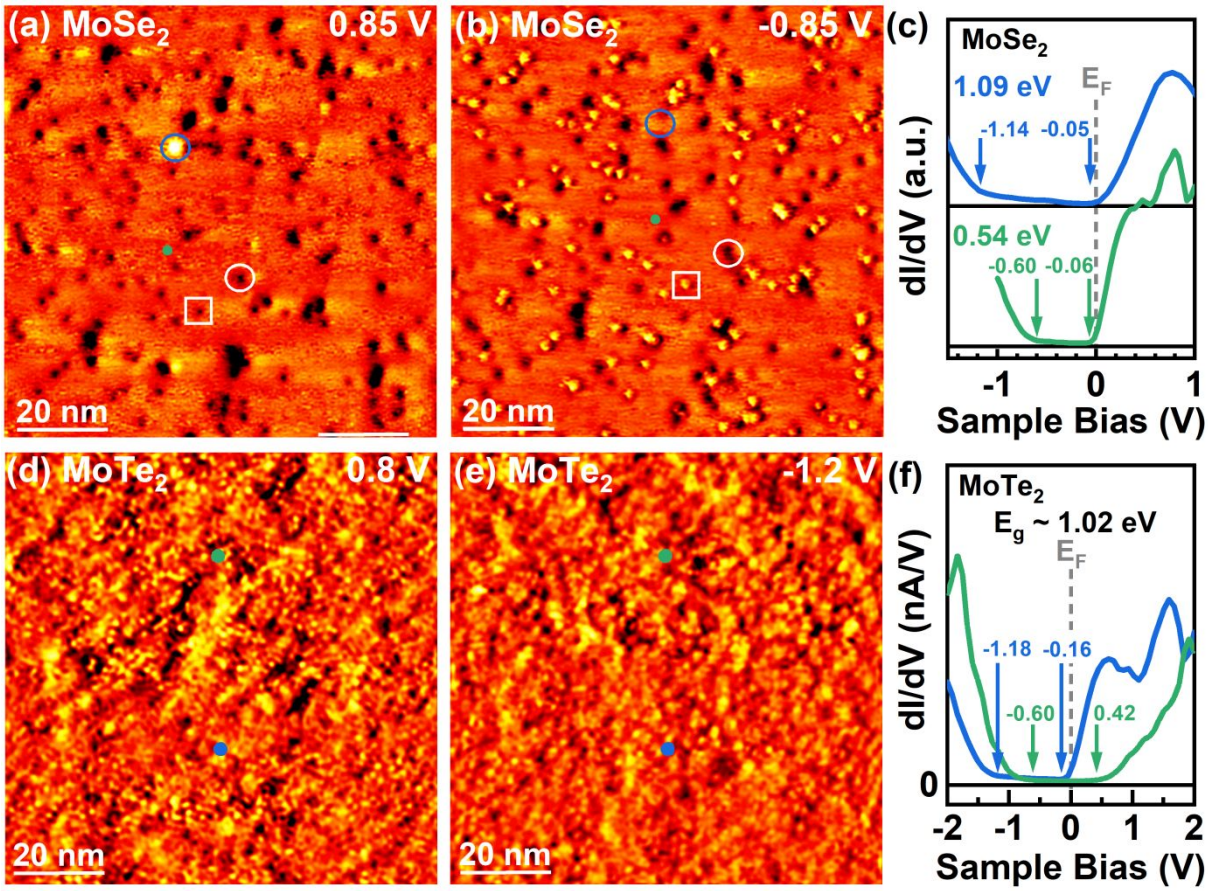

Figure 3. STM images obtained on the same area of a freshly exfoliated $MoSe_2$ bulk crystal surface at (a) 0.85 V, 0.3 nA, (b) -0.85 V, 0.3 nA; (c) STS spectra taken on the surface of $MoSe_2$. The green curve (Eg ~ 0.54 eV) is taken at the green dot shown in (a) and (b). The blue curve (Eg ~ 1.09 eV) is taken at the blue dot in Figure S7c; STM images obtained on the same area of a freshly exfoliated $MoTe_2$ bulk crystal surface at (d) 0.8 V, 0.5 nA, (e) -1.2 V, 0.5 nA; (f) STS spectra (Eg ~ 1.02 eV) taken at the blue and green dots in (d) and (e). The curve and the dot are correlated by the colors.

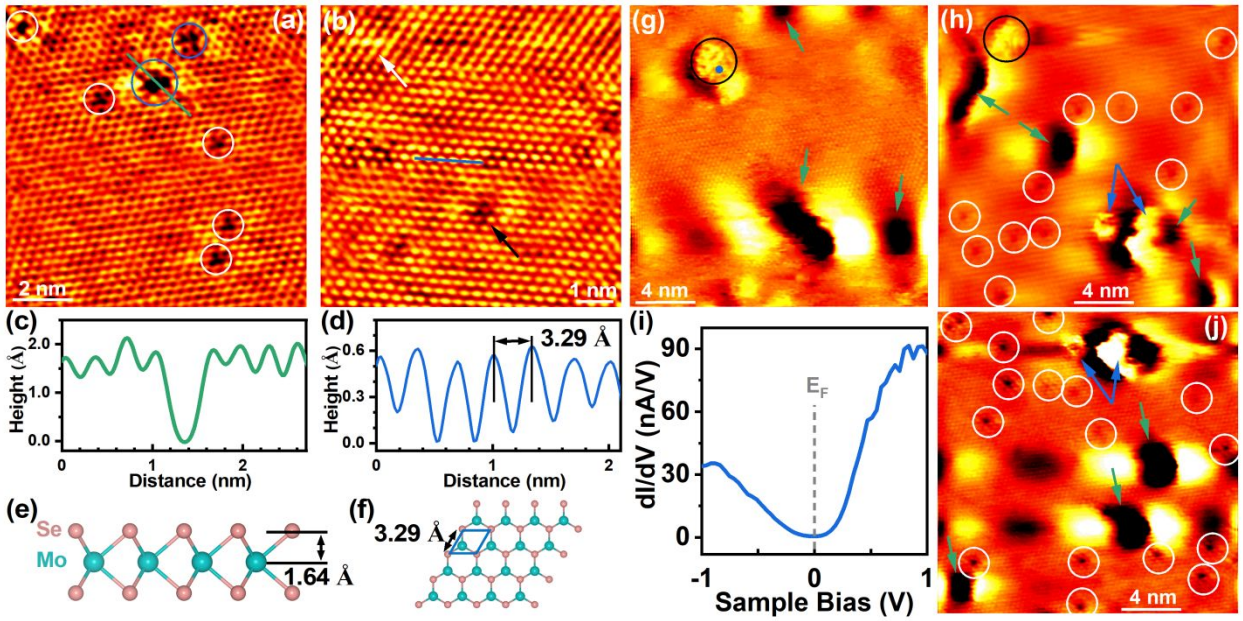

Figure 4. High-resolution STM images of a freshly exfoliated $MoSe_2$ bulk crystal for (a) an area with single (white circle) and multiple (blue circle) V_{Se} and O_{Se}; (b) an area including local high contrast (white arrow) and depression (black arrow); (c) The line profile across the multiple V_{Se} and O_{Se} along the green line in (a); The depth of the V_{Se} or O_{Se} is consistent with the height of 0.5 $MoSe_2$ layers; (d) The line profile along the blue line in (b), the lattice constant of $MoSe_2$ is measured to be ~ 3.29 Å; The (e) side view and (f) top view of $MoSe_2$ lattice; (g), (h), (j) High-resolution STM images of the freshly exfoliated $MoSe_2$ bulk crystal showing local depression (green arrow), bright defect (blue arrow), V_{Se} or O_{Se} (white circle), and disordered protrusion (black circle); (i) dI/dV taken at the disordered protrusion in (g). The band gap is not detectable, indicating a metallic defect.

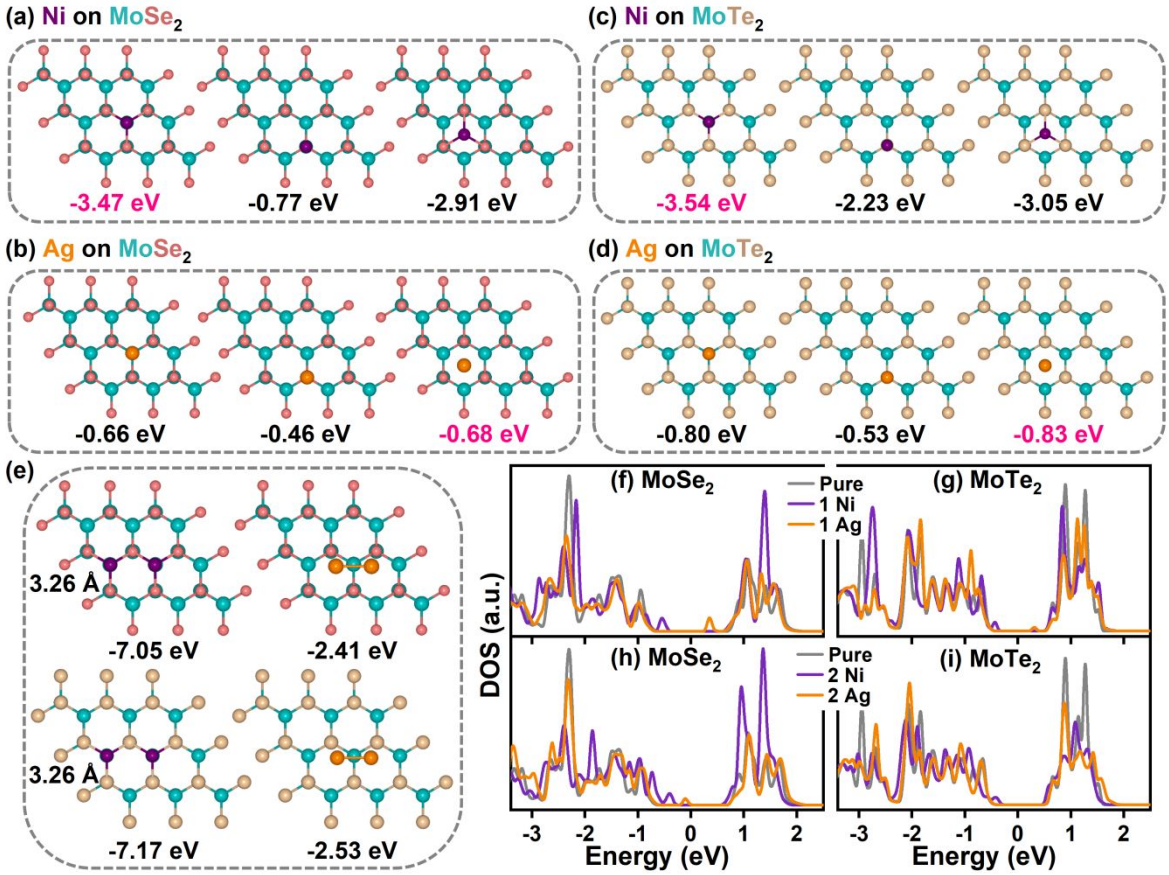

Figure 5. Diagrams of a single (a) Ni atom adsorbed on $MoSe_2$, (b) Ag atom adsorbed on $MoSe_2$, (c) Ni atom adsorbed on $MoTe_2$, and (d) Ag atom adsorbed on $MoTe_2$, with the adsorption energy listed. The adsorption energy of the most stable site is highlighted in pink; (e) two metal atoms adsorbed on Mo-TMDs with the adsorption energy and the distance of the two adatoms listed; DOS plots of a single adatom on the (f) $MoSe_2$ and (g) $MoTe_2$; DOS plots of two adatoms on the (h) $MoSe_2$ and (i) $MoTe_2$.

REFERENCES

(1) Cho, S.; Kim, S.; Kim, J. H.; Zhao, J.; Seok, J.; Keum, D. H.; Baik, J.; Choe, D.-H.; Chang, K. J.; Suenaga, K.; Kim, S. W.; Lee, Y. H.; Yang, H. Phase Patterning for Ohmic Homojunction Contact in $MoTe_2$. *Science* **2015**, *349*, 625.

(2) Bie, Y.-Q.; Grosso, G.; Heuck, M.; Furchi, M. M.; Cao, Y.; Zheng, J.; Bunandar, D.; Navarro-Moratalla, E.; Zhou, L.; Efetov, D. K.; Taniguchi, T.; Watanabe, K.; Kong, J.; Englund, D.; Jarillo-Herrero, P. A $MoTe_2$-Based Light-Emitting Diode and Photodetector for Silicon Photonic Integrated Circuits. *Nat. Nanotechnol.* **2017**, *12*, 1124-1129.

(3) Briggs, N.; Subramanian, S.; Lin, Z.; Li, X.; Zhang, X.; Zhang, K.; Xiao, K.; Geohegan, D.; Wallace, R.; Chen, L.-Q.; Terrones, M.; Ebrahimi, A.; Das, S.; Redwing, J.; Hinkle, C.; Momeni, K.; Van Duin, A.; Crespi, V.; Kar, S.; Robinson, J. A. A Roadmap for Electronic Grade 2D Materials. *2D Mater.* **2019**, *6*, 022001.

(4) Allain, A.; Kang, J.; Banerjee, K.; Kis, A. Electrical Contacts to Two-Dimensional Semiconductors. *Nat. Mater.* **2015**, *14*, 1195-1205.

(5) English, C. D.; Shine, G.; Dorgan, V. E.; Saraswat, K. C.; Pop, E. Improved Contacts to MoS_2 Transistors by Ultra-High Vacuum Metal Deposition. *Nano Lett.* **2016**, *16*, 3824-3830.

(6) McDonnell, S.; Smyth, C.; Hinkle, C. L.; Wallace, R. M. MoS_2–Titanium Contact Interface Reactions. *ACS Appl. Mater. Interfaces* **2016**, *8*, 8289-8294.

(7) Smyth, C. M.; Addou, R.; McDonnell, S.; Hinkle, C. L.; Wallace, R. M. Contact Metal–MoS_2 Interfacial Reactions and Potential Implications on MoS_2-Based Device Performance. *J. Phys. Chem. C* **2016**, *120*, 14719-14729.

(8) Mootheri, V.; Leonhardt, A.; Verreck, D.; Asselberghs, I.; Huyghebaert, C.; de Gendt, S.; Radu, I.; Lin, D.; Heyns, M. Understanding Ambipolar Transport in MoS_2 Field Effect Transistors: The Substrate Is the Key. *Nanotechnology* **2021**, *32*, 135202.

(9) Leonhardt, A.; Chiappe, D.; Asselberghs, I.; Huyghebaert, C.; Radu, I.; Gendt, S. D. Improving MOCVD MoS_2 Electrical Performance: Impact of Minimized Water and Air Exposure Conditions. *IEEE Electron Device Lett.* **2017**, *38*, 1606-1609.

(10) Schoenaers, B.; Leonhardt, A.; Mehta, A. N.; Stesmans, A.; Chiappe, D.; Asselberghs, I.; Radu, I.; Huyghebaert, C.; De Gendt, S.; Houssa, M.; Afanas'ev, V. V. Analysis of Transferred

MoS_2 Layers Grown by MOCVD: Evidence of Mo Vacancy Related Defect Formation. *ECS Journal of Solid State Science and Technology* **2020**, *9*, 093001.

(11) Hong, J.; Hu, Z.; Probert, M.; Li, K.; Lv, D.; Yang, X.; Gu, L.; Mao, N.; Feng, Q.; Xie, L.; Zhang, J.; Wu, D.; Zhang, Z.; Jin, C.; Ji, W.; Zhang, X.; Yuan, J.; Zhang, Z. Exploring Atomic Defects in Molybdenum Disulphide Monolayers. *Nat. Commun.* **2015**, *6*, 6293.

(12) Wang, X.; Kim, S. Y.; Wallace, R. M. Interface Chemistry and Band Alignment Study of Ni and Ag Contacts on MoS_2. *ACS Appl. Mater. Interfaces* **2021**, *13*, 15802–15810.

(13) McDonnell, S.; Addou, R.; Buie, C.; Wallace, R. M.; Hinkle, C. L. Defect-Dominated Doping and Contact Resistance in MoS_2. *ACS Nano* **2014**, *8*, 2880-2888.

(14) Wang, Y.; Chhowalla, M. Making Clean Electrical Contacts on 2D Transition Metal Dichalcogenides. *Nat. Rev. Phys.* **2022**, *4*, 101-112.

(15) Kim, C.; Moon, I.; Lee, D.; Choi, M. S.; Ahmed, F.; Nam, S.; Cho, Y.; Shin, H.-J.; Park, S.; Yoo, W. J. Fermi Level Pinning at Electrical Metal Contacts of Monolayer Molybdenum Dichalcogenides. *ACS Nano* **2017**, *11*, 1588-1596.

(16) Das, S.; Chen, H.-Y.; Penumatcha, A. V.; Appenzeller, J. High Performance Multilayer MoS_2 Transistors with Scandium Contacts. *Nano Lett.* **2013**, *13*, 100-105.

(17) Liu, Y.; Guo, J.; Zhu, E.; Liao, L.; Lee, S.-J.; Ding, M.; Shakir, I.; Gambin, V.; Huang, Y.; Duan, X. Approaching the Schottky–Mott Limit in van der Waals Metal–Semiconductor Junctions. *Nature* **2018**, *557*, 696-700.

(18) Zhang, C.; Li, M.-Y.; Tersoff, J.; Han, Y.; Su, Y.; Li, L.-J.; Muller, D. A.; Shih, C.-K. Strain Distributions and Their Influence on Electronic Structures of WSe_2–MoS_2 Laterally Strained Heterojunctions. *Nat. Nanotechnol.* **2018**, *13*, 152-158.

(19) Song, S.; Keum, D. H.; Cho, S.; Perello, D.; Kim, Y.; Lee, Y. H. Room Temperature Semiconductor–Metal Transition of $MoTe_2$ Thin Films Engineered by Strain. *Nano Lett.* **2016**, *16*, 188-193.

(20) Dong, H.; Gong, C.; Addou, R.; McDonnell, S.; Azcatl, A.; Qin, X.; Wang, W.; Wang, W.; Hinkle, C. L.; Wallace, R. M. Schottky Barrier Height of Pd/MoS_2 Contact by Large Area Photoemission Spectroscopy. *ACS Appl. Mater. Interfaces* **2017**, *9*, 38977-38983.

(21) Wang, Q.; Shao, Y.; Shi, X. Mechanism of Charge Redistribution at the Metal–Semiconductor and Semiconductor–Semiconductor Interfaces of Metal–Bilayer MoS_2 Junctions. *J. Chem. Phys.* **2020**, *152*, 244701.

(22) McClellan, C. J.; Suryavanshi, S. V.; English, C. D.; Smithe, K. K. H.; Bailey, C. S.; Grady, R. W.; Pop, E. 2d Device Trends. http://2d.stanford.edu (accessed February 1 2024).

(23) Kumar, A.; Schauble, K.; Neilson, K. M.; Tang, A.; Ramesh, P.; Wong, H.-S. P.; Pop, E.; Saraswat, K., Sub-200 Ω·μm Alloyed Contacts to Synthetic Monolayer MoS_2. IEEE International Electron Devices Meeting (IEDM), San Francisco, CA, USA, **2021**, pp. 7.3.1-7.3.4

(24) Chou, A.-S.; Cheng, C.-C.; Liew, S.-L.; Ho, P.-H.; Wang, S.-Y.; Chang, Y.-C.; Chang, C.-K.; Su, Y.-C.; Huang, Z.-D.; Fu, F.-Y.; Hsu, C.-F.; Chung, Y.-Y.; Chang, W.-H.; Li, L.-J.; Wu, C.-I. High on-State Current in Chemical Vapor Deposited Monolayer MoS_2 NFETs with Sn Ohmic Contacts. *IEEE Electron Device Lett.* **2021**, *42*, 272-275.

(25) Wang, Y.; Kim, J. C.; Wu, R. J.; Martinez, J.; Song, X.; Yang, J.; Zhao, F.; Mkhoyan, A.; Jeong, H. Y.; Chhowalla, M. van der Waals Contacts between Three-Dimensional Metals and Two-Dimensional Semiconductors. *Nature* **2019**, *568*, 70-74.

(26) O'Brien, K. P.; Dorow, C. J.; Penumatcha, A.; Maxey, K.; Lee, S.; Naylor, C. H.; Hsiao, A.; Holybee, B.; Rogan, C.; Adams, D.; Tronic, T.; Ma, S.; Oni, A.; Gupta, A. S.; Bristol, R.; Clendenning, S.; Metz, M.; Avci, U., Advancing 2D Monolayer CMOS through Contact, Channel and Interface Engineering. IEEE International Electron Devices Meeting (IEDM), San Francisco, CA, USA, 2021, pp. 7.1.1-7.1.4

(27) Shen, P.-C.; Su, C.; Lin, Y.; Chou, A.-S.; Cheng, C.-C.; Park, J.-H.; Chiu, M.-H.; Lu, A.-Y.; Tang, H.-L.; Tavakoli, M. M.; Pitner, G.; Ji, X.; Cai, Z.; Mao, N.; Wang, J.; Tung, V.; Li, J.; Bokor, J.; Zettl, A.; Wu, C.-I.; Palacios, T.; Li, L.-J.; Kong, J. Ultralow Contact Resistance between Semimetal and Monolayer Semiconductors. *Nature* 2021, *593*, 211-217.

(28) Auret, F. D.; Mooney, P. M. Deep Levels Introduced During Electron-Beam Deposition of Metals on N-Type Silicon. *J. Appl. Phys.* 1984, *55*, 988-993.

(29) Chen, C.-H.; Hu, E. L.; Schoenfeld, W. V.; Petroff, P. M. Metallization-Induced Damage in III–V Semiconductors. *J. Vac. Sci. Technol. B* 1998, *16*, 3354.

(30) Haynes, W. M.; Lide, D. R.; Bruno, T. J. *CRC Handbook of Chemistry and Physics, 97th Edition*, CRC Press LLC Taylor & Francis Group: Boca Raton; Florence, 2016.

(31) Dong, H.; Cabrera, W.; Galatage, R. V.; KC, S.; Brennan, B.; Qin, X.; McDonnell, S.; Zhernokletov, D.; Hinkle, C. L.; Cho, K.; Chabal, Y. J.; Wallace, R. M. Indium Diffusion through High-k Dielectrics in High-k/InP Stacks. *Appl. Phys. Lett.* **2013**, *103*, 061601.

(32) Shi, X.; Wang, X.; Sun, Y.; Liu, C.; Wang, W.; Cheng, Y.; Wang, W.; Wang, J.; Cho, K.; Lu, F.; Liu, H.; Dong, H. Interface Chemistry Study of InSb/Al_2O_3 Stacks Upon in situ Post Deposition Annealing by Synchrotron Radiation Photoemission Spectroscopy. *Appl. Surf. Sci.* **2017**, *425*, 932-940.

(33) Yang, L.; Majumdar, K.; Liu, H.; Du, Y.; Wu, H.; Hatzistergos, M.; Hung, P. Y.; Tieckelmann, R.; Tsai, W.; Hobbs, C.; Ye, P. D. Chloride Molecular Doping Technique on 2D Materials: WS_2 and MoS_2. *Nano Lett.* **2014**, *14*, 6275-6280.

(34) Sun, Z.; Pang, C.-S.; Wu, P.; Hung, T. Y. T.; Li, M.-Y.; Liew, S. L.; Cheng, C.-C.; Wang, H.; Wong, H.-S. P.; Li, L.-J.; Radu, I.; Chen, Z.; Appenzeller, J. Statistical Assessment of High-

Performance Scaled Double-Gate Transistors from Monolayer WS_2. *ACS Nano* **2022**, *16*, 14942-14950.

(35) Wang, X.; Hu, Y.; Kim, S. Y.; Addou, R.; Cho, K.; Wallace, R. M. Origins of Fermi Level Pinning for Ni and Ag Metal Contacts on Tungsten Dichalcogenides. *ACS Nano* **2023**, *17*, 20353-20365.

(36) Smyth, C. M.; Addou, R.; Hinkle, C. L.; Wallace, R. M. Origins of Fermi-Level Pinning between Molybdenum Dichalcogenides ($MoSe_2$, $MoTe_2$) and Bulk Metal Contacts: Interface Chemistry and Band Alignment. *J. Phys. Chem. C* **2019**, *123*, 23919-23930.

(37) Kim, J. H.; Lee, J.; Kim, J. H.; Hwang, C. C.; Lee, C.; Park, J. Y. Work Function Variation of MoS_2 Atomic Layers Grown with Chemical Vapor Deposition: The Effects of Thickness and the Adsorption of Water/Oxygen Molecules. *Appl. Phys. Lett.* **2015**, *106*, 251606.

(38) Gong, C.; Colombo, L.; Wallace, R. M.; Cho, K. The Unusual Mechanism of Partial Fermi Level Pinning at Metal–MoS_2 Interfaces. *Nano Lett.* **2014**, *14*, 1714-1720.

(39) Mleczko, M. J.; Yu, A. C.; Smyth, C. M.; Chen, V.; Shin, Y. C.; Chatterjee, S.; Tsai, Y.-C.; Nishi, Y.; Wallace, R. M.; Pop, E. Contact Engineering High-Performance N-Type $MoTe_2$ Transistors. *Nano Lett.* **2019**, *19*, 6352-6362.

(40) Addou, R.; McDonnell, S.; Barrera, D.; Guo, Z.; Azcatl, A.; Wang, J.; Zhu, H.; Hinkle, C. L.; Quevedo-Lopez, M.; Alshareef, H. N.; Colombo, L.; Hsu, J. W. P.; Wallace, R. M. Impurities and Electronic Property Variations of Natural MoS_2 Crystal Surfaces. *ACS Nano* **2015**, *9*, 9124-9133.

(41) Schuler, B.; Lee, J.-H.; Kastl, C.; Cochrane, K. A.; Chen, C. T.; Refaely-Abramson, S.; Yuan, S.; Van Veen, E.; Roldán, R.; Borys, N. J.; Koch, R. J.; Aloni, S.; Schwartzberg, A. M.; Ogletree, D. F.; Neaton, J. B.; Weber-Bargioni, A. How Substitutional Point Defects in Two-Dimensional WS_2 Induce Charge Localization, Spin–Orbit Splitting, and Strain. *ACS Nano* **2019**, *13*, 10520-10534.

(42) Tongay, S.; Zhou, J.; Ataca, C.; Lo, K.; Matthews, T. S.; Li, J.; Grossman, J. C.; Wu, J. Thermally Driven Crossover from Indirect toward Direct Bandgap in 2D Semiconductors: $MoSe_2$ Versus MoS_2. *Nano Lett.* **2012**, *12*, 5576-5580.

(43) Ruppert, C.; Aslan, B.; Heinz, T. F. Optical Properties and Band Gap of Single- and Few-Layer $MoTe_2$ Crystals. *Nano Lett.* **2014**, *14*, 6231-6236.

(44) Addou, R.; Colombo, L.; Wallace, R. M. Surface Defects on Natural MoS_2. *ACS Appl. Mater. Interfaces* **2015**, *7*, 11921-11929.

(45) Mitterreiter, E.; Schuler, B.; Cochrane, K. A.; Wurstbauer, U.; Weber-Bargioni, A.; Kastl, C.; Holleitner, A. W. Atomistic Positioning of Defects in Helium Ion Treated Single-Layer MoS_2. *Nano Lett.* **2020**, *20*, 4437-4444.

(46) Barja, S.; Refaely-Abramson, S.; Schuler, B.; Qiu, D. Y.; Pulkin, A.; Wickenburg, S.; Ryu, H.; Ugeda, M. M.; Kastl, C.; Chen, C.; Hwang, C.; Schwartzberg, A.; Aloni, S.; Mo, S.-K.; Frank Ogletree, D.; Crommie, M. F.; Yazyev, O. V.; Louie, S. G.; Neaton, J. B.; Weber-Bargioni, A. Identifying Substitutional Oxygen as a Prolific Point Defect in Monolayer Transition Metal Dichalcogenides. *Nat. Commun.* **2019**, *10*, 3382.

(47) Stolz, S.; Kozhakhmetov, A.; Dong, C.; Gröning, O.; Robinson, J. A.; Schuler, B. Layer-Dependent Schottky Contact at van der Waals Interfaces: V-Doped WSe_2 on Graphene. *npj 2D Mater. Appl.* **2022**, *6*, 66.

(48) Zhang, K.; Bersch, B. M.; Joshi, J.; Addou, R.; Cormier, C. R.; Zhang, C.; Xu, K.; Briggs, N. C.; Wang, K.; Subramanian, S.; Cho, K.; Fullerton-Shirey, S.; Wallace, R. M.; Vora, P. M.; Robinson, J. A. Tuning the Electronic and Photonic Properties of Monolayer MoS_2 Via in situ Rhenium Substitutional Doping. *Adv. Funct. Mater.* **2018**, *28*, 1706950.

(49) Zheng, H.; Choi, Y.; Baniasadi, F.; Hu, D.; Jiao, L.; Park, K.; Tao, C. Visualization of Point Defects in Ultrathin Layered 1T-$PtSe_2$. *2D Mater.* **2019**, *6*, 041005.

(50) Roy, A.; Movva, H. C. P.; Satpati, B.; Kim, K.; Dey, R.; Rai, A.; Pramanik, T.; Guchhait, S.; Tutuc, E.; Banerjee, S. K. Structural and Electrical Properties of $MoTe_2$ and $MoSe_2$ Grown by Molecular Beam Epitaxy. *ACS Appl. Mater. Interfaces* **2016**, *8*, 7396-7402.

(51) James, P. B.; Lavik, M. T. The Crystal Structure of $MoSe_2$. *Acta Crystallogr.* **1963**, *16*, 1183-1183.

(52) Costa-Amaral, R.; Forhat, A.; Caturello, N. A. M. S.; Silva, J. L. F. D. Unveiling the Adsorption Properties of 3d, 4d, and 5d Metal Adatoms on the MoS_2 Monolayer: A DFT-D3 Investigation. *Surf. Sci.* **2020**, *701*, 121700.

(53) Chen, J.; Zhang, Z.; Guo, Y.; Robertson, J. Metal Contacts with Moire Interfaces on WSe_2 for Ambipolar Applications. *Appl. Phys. Lett.* **2022**, *121*, 051602.

(54) Brillson, L. J. Transition in Schottky Barrier Formation with Chemical Reactivity. *Phys. Rev. Lett.* **1978**, *40*, 260-263.

(55) Edelberg, D.; Rhodes, D.; Kerelsky, A.; Kim, B.; Wang, J.; Zangiabadi, A.; Kim, C.; Abhinandan, A.; Ardelean, J.; Scully, M.; Scullion, D.; Embon, L.; Zu, R.; Santos, E. J. G.; Balicas, L.; Marianetti, C.; Barmak, K.; Zhu, X.; Hone, J.; Pasupathy, A. N. Approaching the Intrinsic Limit in Transition Metal Diselenides Via Point Defect Control. *Nano Lett.* **2019**, *19*, 4371-4379.

(56) HQ Graphene. www.hqgraphene.com (accessed 01 February 2023).

(57) Wallace, R. M. In-Situ Studies of Interfacial Bonding of High-k Dielectrics for CMOS Beyond 22nm. *ECS Trans.* **2008**, *16*, 255-271.

(58) The University of Texas at Dallas Cleanroom https://cleanroom.utdallas.edu/ (accessed 01 February 2023).

(59) ASTM E2108-16. *Standard Practice for Calibration of the Electron Binding Energy Scale of an X-Ray Photoelectron Spectrometer* **2016** (West Conshohocken, PA: ASTM) https://doi.org/10.1520/E2108-16.

(60) Herrera-Gómez, A.; Hegedus, A.; Meissner, P. L. Chemical Depth Profile of Ultrathin Nitrided SiO_2 Films. *Appl. Phys. Lett.* **2002**, *81*, 1014-1016.

(61) Wang, X.; Cormier, C. R.; Khosravi, A.; Smyth, C. M.; Shallenberger, J. R.; Addou, R.; Wallace, R. M. In Situ Exfoliated 2D Molybdenum Disulfide Analyzed by XPS. *Surf. Sci. Spectra* **2020**, *27*, 014019.

(62) Horcas, I.; Fernández, R.; Gómez-Rodríguez, J. M.; Colchero, J.; Gómez-Herrero, J.; Baro, A. M. WSxM: A Software for Scanning Probe Microscopy and a Tool for Nanotechnology. *Rev. Sci. Instrum.* **2007**, *78*, 013705.

(63) Nečas, D.; Klapetek, P. Gwyddion: An Open-Source Software for SPM Data Analysis. *Open Physics* **2012**, *10*, 181–188.

(64) Kresse, G.; Furthmüller, J. Efficiency of Ab-Initio Total Energy Calculations for Metals and Semiconductors Using a Plane-Wave Basis Set. *Comput. Mater. Sci.* **1996**, *6*, 15-50.

(65) Kresse, G.; Hafner, J. Ab Initio Molecular Dynamics for Liquid Metals. *Phys. Rev. B* **1993**, *47*, 558-561.

(66) Kresse, G.; Hafner, J. Norm-Conserving and Ultrasoft Pseudopotentials for First-Row and Transition Elements. *J. Phys.: Condens. Matter* **1994**, *6*, 8245.

(67) Kresse, G.; Joubert, D. From Ultrasoft Pseudopotentials to the Projector Augmented-Wave Method. *Phys. Rev. B* **1999**, *59*, 1758-1775.

(68) Perdew, J. P.; Chevary, J. A.; Vosko, S. H.; Jackson, K. A.; Pederson, M. R.; Singh, D. J.; Fiolhais, C. Atoms, Molecules, Solids, and Surfaces: Applications of the Generalized Gradient Approximation for Exchange and Correlation. *Phys. Rev. B* **1992**, *46*, 6671.

(69) Perdew, J. P.; Burke, K.; Ernzerhof, M. Generalized Gradient Approximation Made Simple. *Phys. Rev. Lett.* **1996**, *77*, 3865.

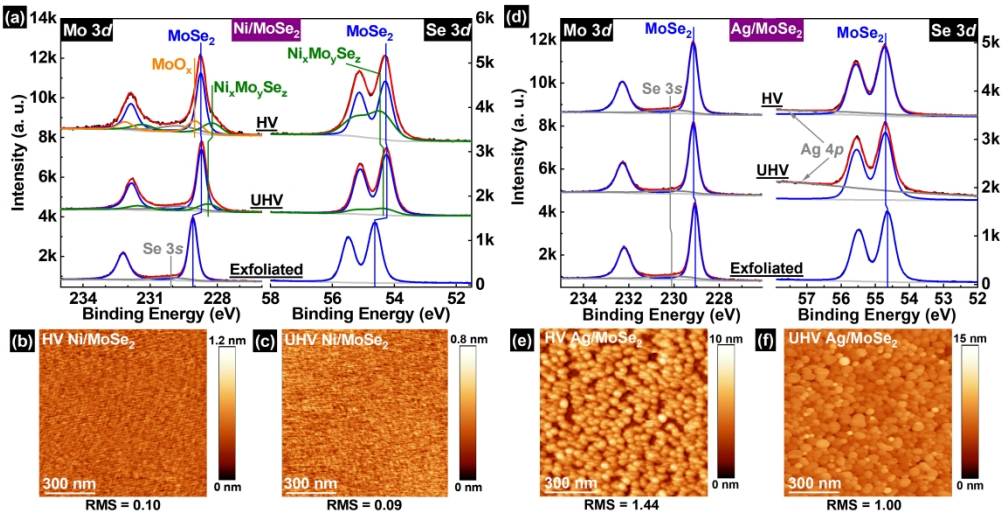

Figure 1. Mo 3d and Se 3d spectra of $MoSe_2$ bulk crystal following exfoliation and subsequent (a) Ni, and (d) Ag depositions under UHV and HV conditions. AFM results of Ni/$MoSe_2$ bulk crystal surfaces deposited under (b) HV and (c) UHV conditions. AFM results of Ag/$MoSe_2$ bulk crystal surfaces deposited under (e) HV and (f) UHV conditions. The unit of RMS roughness is nm.

175x91mm (600 x 600 DPI)

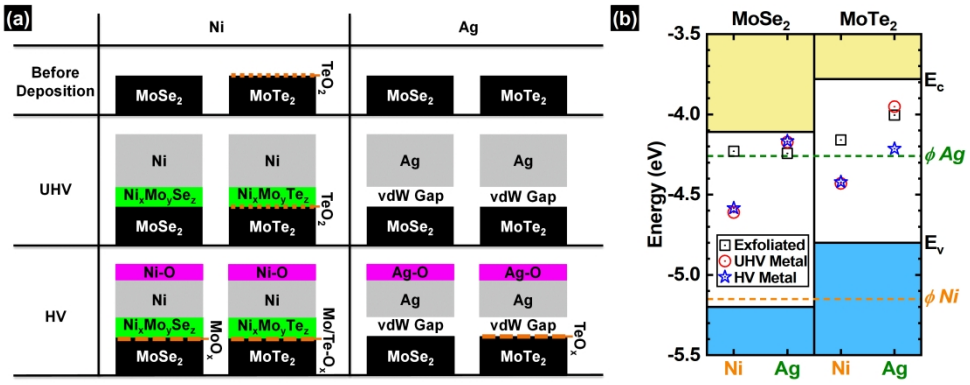

Figure 2. (a) Schematic representations of the interfaces formed between contact metals (Ni and Ag) and TMDs ($MoSe_2$ and $MoTe_2$) before and after metal depositions under UHV and HV conditions. (b) Band alignment of contact metal/TMD bulk crystal systems studied in this work after exfoliation and subsequent metal deposition under UHV and HV conditions.

172x65mm (600 x 600 DPI)

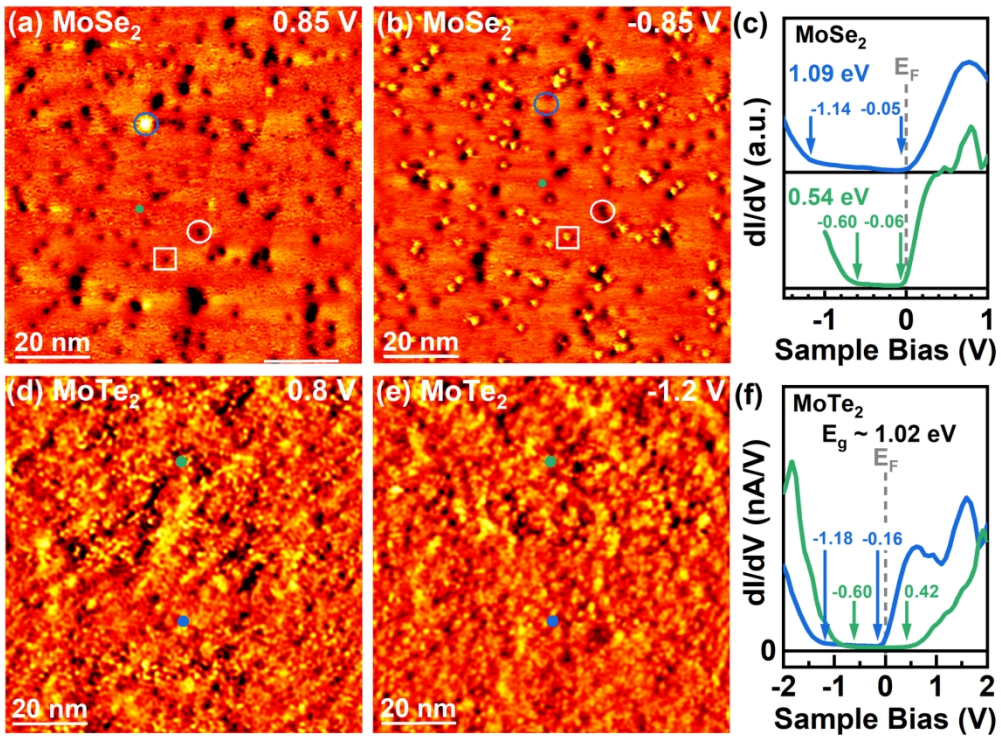

Figure 3. STM images obtained on the same area of a freshly exfoliated $MoSe_2$ bulk crystal surface at (a) 0.85 V, 0.3 nA, (b) -0.85 V, 0.3 nA; (c) STS spectra taken on the surface of $MoSe_2$. The green curve (E_g ~ 0.54 eV) is taken at the green dot shown in (a) and (b). The blue curve (E_g ~ 1.09 eV) is taken at the blue dot in Figure S7c; STM images obtained on the same area of a freshly exfoliated $MoTe_2$ bulk crystal surface at (d) 0.8 V, 0.5 nA, (e) -1.2 V, 0.5 nA; (f) STS spectra (E_g ~ 1.02 eV) taken at the blue and green dots in (d) and (e). The curve and the dot are correlated by the colors.

160x118mm (300 x 300 DPI)

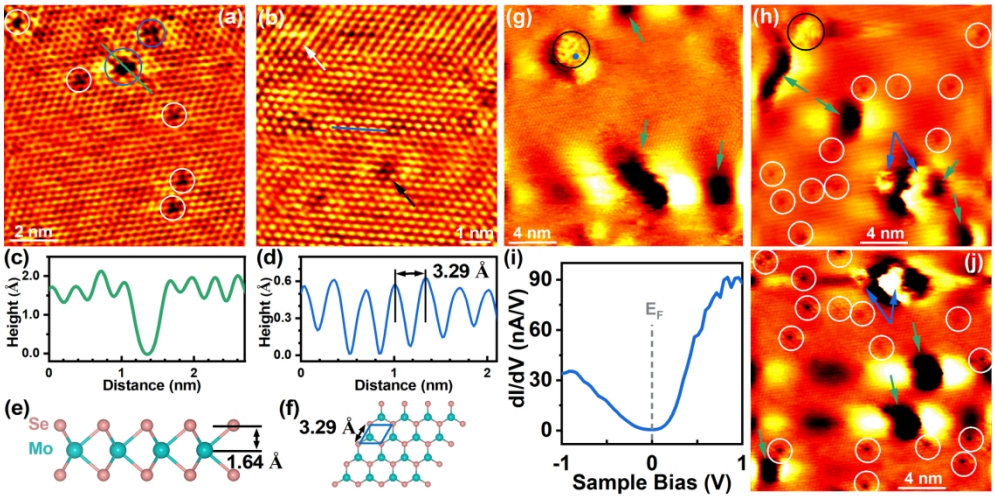

Figure 4. High-resolution STM images of a freshly exfoliated $MoSe_2$ bulk crystal for (a) an area with single (white circle) and multiple (blue circle) V_{Se} and O_{Se}; (b) an area including local high contrast (white arrow) and depression (black arrow); (c) The line profile across the multiple V_{Se} and O_{Se} along the green line in (a); The depth of the V_{Se} or O_{Se} is consistent with the height of 0.5 $MoSe_2$ layers; (d) The line profile along the blue line in (b), the lattice constant of $MoSe_2$ is measured to be ~ 3.29 Å; The (e) side view and (f) top view of $MoSe_2$ lattice; (g), (h), (j) High-resolution STM images of the freshly exfoliated $MoSe_2$ bulk crystal showing local depression (green arrow), bright defect (blue arrow), V_{Se} or O_{Se} (white circle), and disordered protrusion (black circle); (i) dI/dV taken at the disordered protrusion in (g). The bandgap is not detectable, indicating a metallic defect.

169x84mm (300 x 300 DPI)

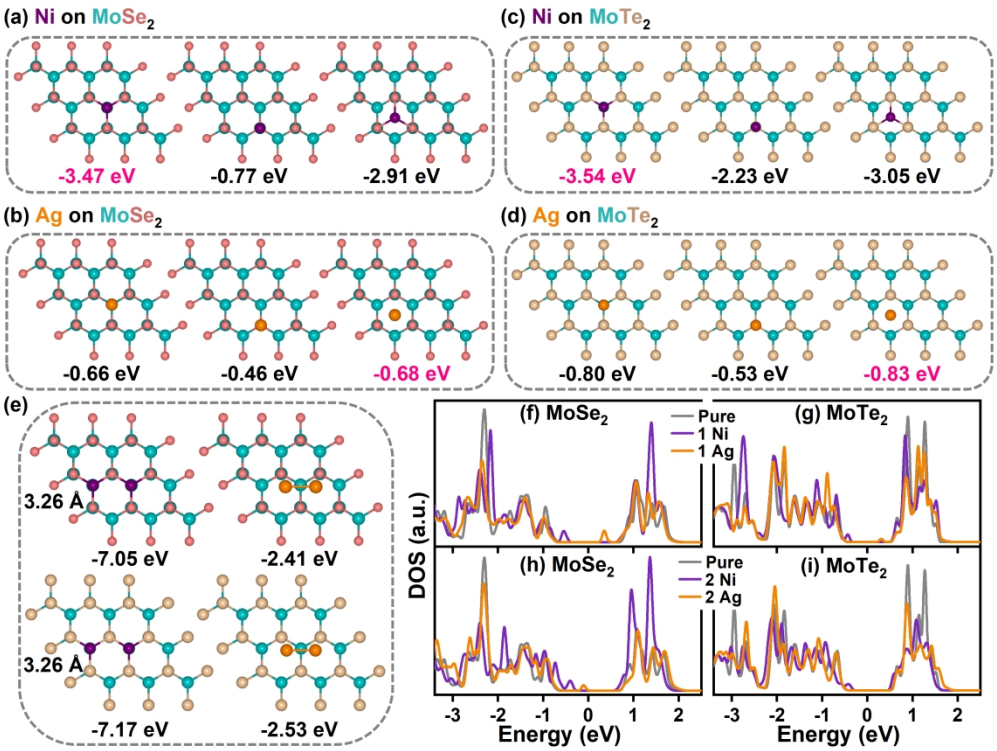

Figure 5. Diagrams of a single (a) Ni atom adsorbed on $MoSe_2$, (b) Ag atom adsorbed on $MoSe_2$, (c) Ni atom adsorbed on $MoTe_2$, and (b) Ag atom adsorbed on $MoTe_2$, with the adsorption energy listed. The adsorption energy of the most stable site is highlighted in pink; (e) two metal atoms adsorbed on Mo-TMDs with the adsorption energy and the distance of the two adatoms listed; DOS plots of a single adatom on the (f) $MoSe_2$ and (g) $MoTe_2$; DOS plots of two adatoms on the (h) $MoSe_2$ and (i) $MoTe_2$.

154x116mm (600 x 600 DPI)

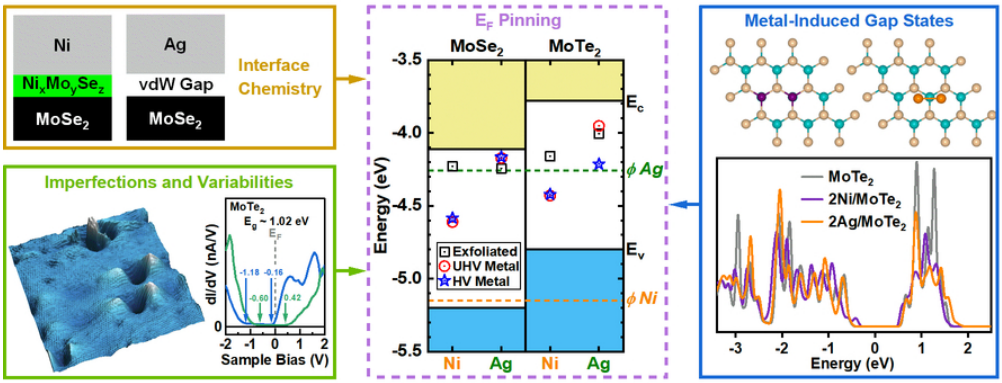

Table of Contents Figure

75x28mm (300 x 300 DPI)